Observation of atmospheric and oceanic dynamics using ocean-bottom distributed acoustic sensing

Kittinat Taweesintananon[1,2], Martin Landrø[1], Ståle Emil Johansen[3], John Robert Potter[1], Robin André Rørstadbotnen[1], Léa Bouffaut[1]*, Hannah Joy Kriesell[1], Jan Kristoffer Brenne[4], Aksel Haukanes[4]†, Olaf Schjelderup[5]‡, and Frode Storvik[5]‡

[1]Acoustics Group, Department of Electronic Systems, Norwegian University of Science and Technology (NTNU), Trondheim 7491, Norway.

[2]PTT Exploration and Production Public Company Limited (PTTEP), Bangkok 10900, Thailand.

[3]Department of Geoscience and Petroleum, Norwegian University of Science and Technology (NTNU), Trondheim 7491, Norway.

[4]Alcatel Submarine Networks Norway AS, Tiller 7075, Norway.

[5]Uninett AS, Trondheim 7030, Norway.

Corresponding author: Kittinat Taweesintananon (kittinat.taweesintananon@ntnu.no)

*Léa Bouffaut is now at K. Lisa Yang Center for Conservation Bioacoustics, Cornell Lab of Ornithology, Cornell University, Ithaca, NY 14850, USA.

†Aksel Haukanes is now at Leirvik AS, Stord 5416, Norway.

‡From 2022-01-01, Uninett AS is a part of Sikt, Trondheim 7030, Norway.

Key Points:

- We review the mechanisms of ocean-bottom seismo-acoustics recorded by Distributed Acoustic Sensing (DAS) of seafloor telecommunication fiber-optic cables.
- We are able to trace primary microseisms measured by DAS back to distant storms more than 10,000 km away.
- DAS could be a valuable and game-changing addition to the Global Ocean Observing System (GOOS), expanding coverage, spatial and temporal resolution.

Abstract

Distributed Acoustic Sensing (DAS) leverages an ocean-bottom telecommunication fiber-optic cable into a densely-sampled massive array of strain sensors. We demonstrate DAS applications to Passive Acoustic Monitoring (PAM) through an experiment in Longyearbyen, Svalbard, Norway. We show that DAS can measure many types of signals generated by dynamics in the atmosphere, ocean, and solid earth. These include primary and secondary microseisms, Scholte waves, water-layer acoustic resonances, and seismic waves from earthquakes. In addition, we can trace the origin of primary microseisms back to distant storms a quarter of the way around the planet. We also find that the fjord acts as an amplifier for microseisms. Because DAS is capable of hydroacoustic monitoring with high spatial resolution over great distances, it can deliver great scientific value to ocean observation. We believe that DAS can and will become a valuable component of the Global Ocean Observing System.

Plain Language Summary

Over 1.3 million kilometers of submarine fiber-optic cables have been deployed around the Earth for telecommunications. In this study, we use one such cable in Svalbard, Norway, to measure vibrations at the seafloor. We describe the characteristics of these signals and deduce their origins, which include distant storms occurring in the South Atlantic Ocean more than 10,000 km away. We believe that this sensing technique will soon become a standard and powerful tool for the oceanographic community.

1 Introduction

The Earth's atmosphere and oceans are continuously in coupled motion. These complex motions and interactions determine both weather and, over the longer term, the climate of the planet. Oceans play a highly significant role in climate, because they can retain heat and distribute it around the globe (Schmitt, 2018). Large-scale ocean currents, which are driven by variations in water density caused by temperature and salinity gradients, influence the climate by exchanging heat and water with the atmosphere. A change in ocean dynamics could induce major climate variations over large areas of the Earth in the long term (Bigg & Hanna, 2016). Hence, ocean surface winds, currents, and surface gravity waves are key climate variables that induce exchanges of momentum, energy, heat, salinity, gases, and other tracers between the ocean and atmosphere (Villas Bôas et al., 2019).

Ocean surface gravity waves have random properties and evolve from complex mechanisms. Their modern studies started in the 1940s (Mitsuyasu, 2002; Wunsch, 2021), with seminal contributions from icons such as Sverdrup (Sverdrup, 1947), Stommel (Stommel, 1948) and Munk (Munk, 1950). Ocean surface gravity waves are a primary source of turbulence in the upper ocean, and they are an important factor in the air-sea momentum transfer. In addition, they directly affect navigation, offshore structure design, and coastal erosion (Abolfazli et al., 2020). However, they are not used explicitly in constraining most ocean-atmosphere models, because high-spatial-resolution (scales under 25 km) two-dimensional (2D) measurements of waves are not normally available. Such measurements could significantly improve ocean models (Wu et al., 2019).

Many instruments have been developed to measure directional ocean surface gravity waves (European cooperation in science and technology Action 714, Working Group 3, 2005). The classical methods such as spatial arrays and pitch-and-roll buoys have been complemented by new technologies such as the displacement and GPS buoys, acoustic Doppler current meters, microwave and marine radars, coastal high-frequency radars, and real and synthetic aperture radars. However, none of these instruments can provide all the data needed to make a complete and robust estimate of the directional properties of ocean surface gravity waves. Data with high spatial resolution and extensive spatial coverage would be necessary to overcome this limit. In principle, subsurface instruments that measure ocean-bottom pressure fluctuations due to surface gravity waves could be deployed in spatially extended arrays for accurate estimation of swell directional spectra, but this would be prohibitively expensive. Therefore, compact subsurface instruments, whose dimensions are smaller than the typical wavelength, are more widely used by the oceanographic community.

Distributed Acoustic Sensing (DAS) is a technology that is able to exploit the optical fiber in standard telecommunication cables as an extended spatial array of acoustic sensors (Hartog, 2017). Over 1.3 million kilometers of submarine telecommunication cables have been deployed around the Earth. Many optical fibers in these cables, often 'spares', are not currently used for telecommunication. It is possible to repurpose these unused 'dark' fibers to serve as distributed acoustic sensors to measure, among other signals, ocean-bottom pressure fluctuations. DAS measures the strain fluctuations at each sensing element of an optical fiber. A DAS interrogator can measure the strain data along the fiber with a length up to 171 km (Waagaard et al., 2021). Therefore, DAS can form spatially extended arrays with very large dimension compared to the typical length of ocean surface gravity waves. In addition, DAS measures data with a spatial sampling interval of as little as 1 m, which creates arrays of many tens of thousands of sensors at low cost.

DAS in submarine fiber-optic cables can measure pressure fluctuations at the ocean bottom originating from a variety of sources (Landrø et al., 2021). DAS in ocean-bottom telecommunication cables can detect ocean surface gravity waves, microseisms and earthquakes (Lindsey et al., 2019; Sladen et al., 2019). Furthermore, Williams et al. (2019) demonstrate that DAS can record the seismic waves from a distant earthquake, ocean surface gravity waves, and Scholte waves. However, their spectral analyses were performed on a data record of only one-hour. DAS data with a longer recording length are necessary for studying the dynamics of ocean surface gravity waves originating from distant storms. For example, Zhan et al. (2021) show several dispersive signals from ocean swells from distant storms in a spectrogram computed over 11 days of the fiber-optic sensing data using the state of polarization technique.

In this article, we show that DAS can be employed as a valuable tool for studying ocean dynamics. First, we describe the DAS data used in our study and their acquisition parameters. Second, we review the mechanisms of the ocean-bottom vibrations that are recorded by DAS along an ocean-bottom telecommunication cable. We also review the characteristics of the DAS data corresponding to different mechanisms of the ocean-bottom vibrations. Then, we discuss the results of our analysis related to ocean surface gravity waves corresponding to distant storms. Finally, we address some potential applications of DAS in the oceanographic community.

2 Method

We used a dark fiber of SMF-28 single mode silica type in an existing submarine telecommunication cable, which was trenched into soft sediments at 0–2 m below the seafloor, from Longyearbyen to Ny-Ålesund in Svalbard, Norway (Figure 1). The cable is owned and operated by Uninett AS, which is the National Research and Education Network (NREN) in

Norway. We connected an OptoDAS interrogator, developed by Alcatel Submarine Networks, to the cable end onshore Longyearbyen. The OptoDAS interrogator sends linear optical frequency-modulated swept pulses into the fiber and receives backscattered pulses from impurities in the fiber (Waagaard et al., 2021). It calculates the time-differentiated phase changes of consecutive backscattered pulses corresponding to every spatially sampled position along the fiber. These are used to estimate longitudinal strains of the fiber at each sampling point. In this experiment, we use light pulses with a free-space wavelength of 1,550 nm and a sampling period of 1×10^{-8} s at the optical receiver. Defined by regions of interest, we extract 30,000 channels sampled every 4.08 m along the fiber from 0 to 120 km from the interrogator. Figure 1 shows a map of the DAS array used in our experiment. The DAS data was continuously recorded using 1.55 ms time sampling interval throughout the survey. The spatial sampling interval is 1.02 m, while the gauge length is 8.16 m. The backscattered signal strength decays by ≈ 0.2 dB/km along the cable, amounting to -40 dB over 100 km. The data were acquired over 44 days from 2020-06-23 to 2020-08-04.

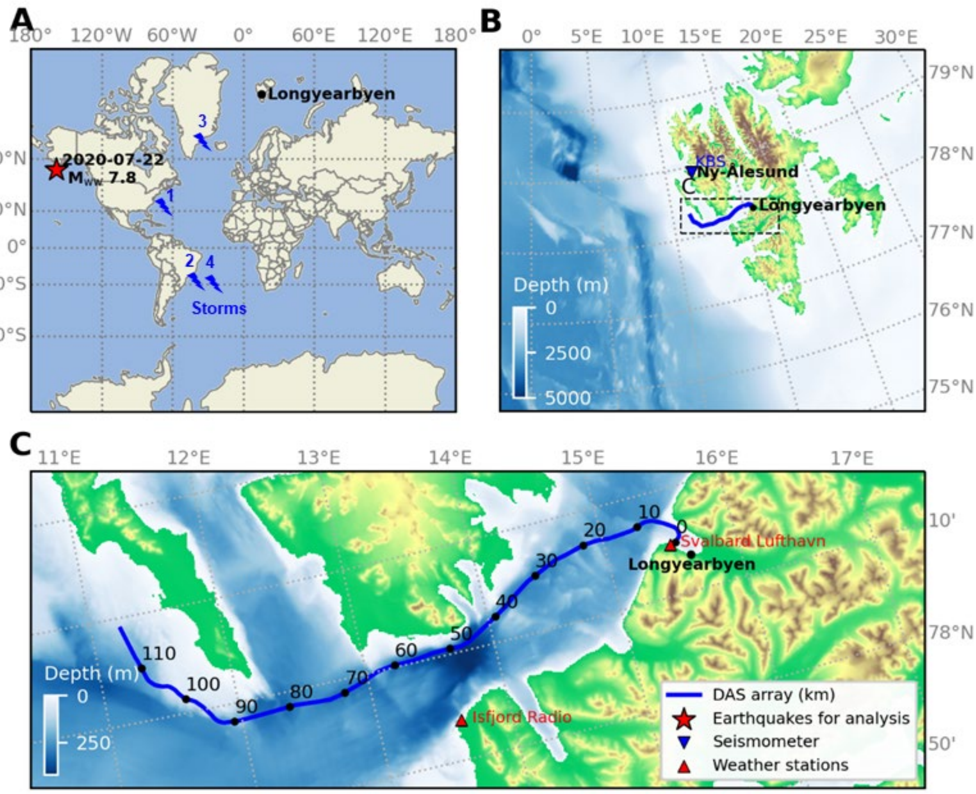

Figure 1. Maps of the seabed DAS array. A World map showing the array location in Longyearbyen, the epicenter of the 2020-07-22 M_{ww} 7.8 earthquake on the Alaska Peninsula, and the approximate storm locations marked in Figure 4C. **B** Regional map showing the array and the KBS seismic station. **C** Local map showing the array annotated with the distance in km from the shore in Longyearbyen, and nearby weather stations.

The phenomena investigated in this study occur below 20 Hz. Therefore, we resample the DAS strain data from 1.55 to 20 ms with the antialiasing filter at 80% of the output Nyquist frequency. The resampled data with the Nyquist frequency of 25 Hz are used in our analysis. Data resampling also reduces the computational cost for analyzing data over a long-time window. We also attenuate interrogator noise that occurs in the whole DAS array, where the noise model is obtained by stacking all the DAS data traces from onshore channels in a calm environment. To understand the characteristics of the data corresponding to different mechanisms of the ocean-bottom vibrations, we compare the processed data with and without the excitation from seismic waves. With this comparison, we can distinguish the microseisms from other ocean-bottom pressure responses measured by DAS.

2.1 Mechanisms of ocean-bottom vibrations

The strain of a fiber section will be proportional to that component of the pressure gradient projected along the direction of the fiber. Pressure changes in space and time are therefore detectable by DAS at the seabed, providing they cause strains above the detection limit (due to noise) in the order of 1 nε. Ocean-bottom vibrations corresponding to pressure changes can be caused by four excitation mechanisms (Saito & Tsushima, 2016):

1. Fluctuation of either sea-surface height or water density causing changes in the ocean-bottom loading pressure. This hydrostatic pressure response is called a microseism, and it is associated with ocean surface gravity waves generated by winds and nonlinear wave-wave interaction mechanisms.
2. Fluctuation of the vertical seabed placement also causes changes in the ocean-bottom loading pressure. This pressure response contributes another hydrostatic response due to gravity.
3. Hydrodynamic responses associated with the interaction of propagating seismic waves at the seafloor interface between seawater and the solid earth.
4. Forces generated by the compressibility of seawater and the elasticity of the ocean-bottom rock causes a hydroacoustic response associated with the acoustic resonance of the P-wave propagating within the water layer, resulting in different normal modes.

A primary microseism is driven by ocean surface gravity waves. Hence, the phase velocity (c_p) of the primary microseism is given by $c_p = \omega/k$ with the dispersive relation $\omega^2 = gk\tanh(kH)$, where $\omega = 2\pi f$ is the angular frequency, $k = 2\pi/\lambda$ is the angular wavenumber, $g \approx 9.81\ \mathrm{m/s^2}$ is the gravitational acceleration, and H is the water depth (Airy, 1841; Craik, 2004). According to linear wave theory (Dean & Dalrymple, 1991, sec. 3.4.4), the dispersive relation for deep water ($H > 0.5\,\lambda$) reduces to $\omega^2 \approx gk$, while the relation for shallow water ($H < 0.05\,\lambda$) reduces to $\omega^2 \approx gk^2H$.

Matsumoto et al. (2012) comprehensively describe the frequency ranges of three pressure responses at the seabed: hydrostatic, hydrodynamic, and hydroacoustic. First, for a given wavelength, the frequency of an ocean surface gravity wave occurs in deep water at $f \approx \sqrt{g/(2\pi\lambda)}$. We may approximately derive the frequency (f_d) in deep water as a function of water depth by assuming $H = 0.5\,\lambda$, which is the lower limit of deep-water depth. Hence, the frequency limit of ocean surface gravity waves in deep water as a function of water depth is approximately defined by

$$f_d = \frac{1}{2}\sqrt{\frac{g}{\pi H}}\ . \tag{1}$$

Assuming $H = 0.05\,\lambda$ for the upper limit of shallow water depth, we can derive the frequency (f_s) of an ocean surface gravity wave in shallow water from $f \approx \sqrt{gH/\lambda^2}$:

$$f_s = \frac{1}{20}\sqrt{\frac{g}{H}} \ . \tag{2}$$

A primary microseism is the direct hydrostatic pressure response onto the seafloor corresponding to an ocean surface gravity wave; hence, it has the same frequency as the ocean surface wave. When primary microseism wave trains (ocean surface gravity waves) propagate in opposite directions (as occurs on reflection from topography, for example), secondary microseisms can be generated by non-linear wave-wave interaction at double the frequency of the primary microseism (Ardhuin & Herbers, 2013). Second, the lower frequency limit of the hydroacoustic responses is governed by the fundamental (the 1st order) acoustic resonant frequency as formulated by $f_1 = c/(4H)$. Acoustic resonant frequencies are expressed as the cut-off (lower limit) frequency for normal modes:

$$f_n = \frac{(2n-1)c}{4H} \ , \tag{3}$$

where n is a positive integer indicating the order of the normal mode and c is the acoustic velocity in the water (Landrø & Hatchell, 2012). Last, the hydrodynamic responses associated with the seismic waves from an earthquake can be pronounced in a wide frequency range depending on the seismic source and the elastic properties of the subsurface. Unlike hydrostatic and hydroacoustic responses, the frequency of hydrodynamic responses from seismic waves is independent of water depth.

2.2 Origin of ocean swells

Ocean surface gravity waves are generated by friction exerted by wind on the ocean surface. Propagating waves are generated when the restoration of the fluid to equilibrium is driven by gravity. Wave size depends on wind speed, wind duration and the area over which the wind is blowing (the fetch). Large ocean surface gravity waves generated by storms can propagate for a long distance. These waves are also called ocean swells.

Ocean-bottom seismic sensors can detect ocean swells generated from large storms occurring several thousand kilometers away. Bromirski & Duennebier (2002) discuss the amplitude characteristics and wave spectra of these microseisms. The dispersion relation for ocean surface gravity waves in deep water predicts that low-frequency waves will arrive before higher-frequency waves. Also, it depicts the resulting linear up-sweep characteristics of ocean swells in spectrograms (time-frequency representations) computed from ocean-bottom seismic data (Bromirski & Duennebier, 2002, fig. 11). Using the method described in Lin et al. (2018) based on Munk et al. (1963), we can also trace ocean swells, measured by DAS, back to their originating distant storms. We use the time-frequency gradients measured in spectrograms to calculate the great-circle distances and travel times of the storm-induced ocean swells traveling from the storm centers to the DAS receiver.

Lin et al. (2018) derive the expression for the propagation distance of an ocean swell, based on Munk et al. (1963) as

$$x = \frac{g}{4\pi\left(\frac{df}{dt}\right)} \ , \tag{4}$$

where f is the frequency of the primary microseism associated with an ocean swell. Here, df/dt is the time-frequency gradient or slope of the linear up-sweep trend. Further, the group velocity (c_g) of an ocean surface gravity wave in deep water can be computed from

$$c_g = \frac{1}{2}\sqrt{\frac{g}{k}} \approx \frac{g}{4\pi f} \,, \tag{5}$$

where f is the frequency of the wave. We can, then, estimate the travel time (t) of the ocean swell from the storm center to the DAS receiver from

$$t = \frac{x}{c_g} \,. \tag{6}$$

In short, we firstly estimate the slope of a linear up-sweep trend in the spectrogram and determine the propagation distance of the swell using equation (4). Next, we use the start frequency of the trend in the spectrogram to compute the group velocity and the travel time using equations (5) and (6), respectively. The estimated distance and travel time help to characterize the storms that produced the observed ocean swells.

3 Results and discussion

3.1 Data characterization

On 2020-07-22 at 06:12:44 (UTC), an earthquake with a moment W-phase magnitude (M_{ww}) of 7.8 occurred at a depth of 28 km approximately 100 km south of the Alaska Peninsula (Figure 1A). The earthquake was detected by seismic stations worldwide and our DAS array near Longyearbyen, which is approximately 5,100 km away from the epicenter on a great circle. At the DAS channel at 36 km inline distance from the shore, the approximate arrival times of the P-, S- and SS-waves are respectively at 510, 950 and 1200 s from the earthquake's origin time. We compare the data in the 1200-s time windows before and after 2020-07-22T06:20:02Z, which is the timestamp at 72, 512 and 762 s before the first arrivals of P-, S- and SS-waves, respectively.

Figures 2A and 2B show the spectral analysis from 0.01 to 20 Hz of processed DAS strain data from the 1200-s time window before the seismic event. Note that the processed data have a time sampling interval of 20 ms, i.e., the Nyquist frequency is 25 Hz. A power spectrum is computed by a discrete Fourier transform along the time axis of the processed data within the whole 1200-s time window, in which the normalization factor is 1 (unscaled) for the forward transform. The average power spectra over 251 channels (500 m radius) around three selected locations are shown in Figure 2A. The locations are selected to represent the data recorded at different water depths and distances from the shore. The power spectra of individual channels are combined to produce the distance-frequency plot in Figure 2B. There are four energy peaks (Events 1 to 4 marked in Figure 2A) in the spectra within 5 km from shore where the water is less than 100 m deep (see water depth profile in Figure 3D). Only two of these energy peaks are present where the water depth is greater than 100 m. The input strain data used in the spectral analysis are given in Figure S1 for reference.

The 0.06-Hz peak (Event 1 in Figure 2A) present in all water depths corresponds to primary microseisms associated with ocean surface gravity waves, excited by either local winds or distant storms. The frequency of the primary microseisms visible in the figure has weak or no correlation with water depth and the waves are seen to propagate towards the shore, illustrated by the temporal-spatial correlations in Figure 3C. Figure 3C also shows that in shallow water near the shore, reflected waves propagate in the opposite direction. These two wave trains with the same frequency, propagating in opposite directions, generate the 0.12-Hz energy peak harmonic in the power spectra (Event 2 in Figure 2A) as discussed in Hasselmann (1963). Hence, the 0.12-Hz energy peak is a secondary microseism, generated only in shallow water, of twice the fundamental primary microseism frequency. These reflected waves are not apparent in water deeper than 100 m, so the secondary microseism is only observable near shore with water depth <100 m.

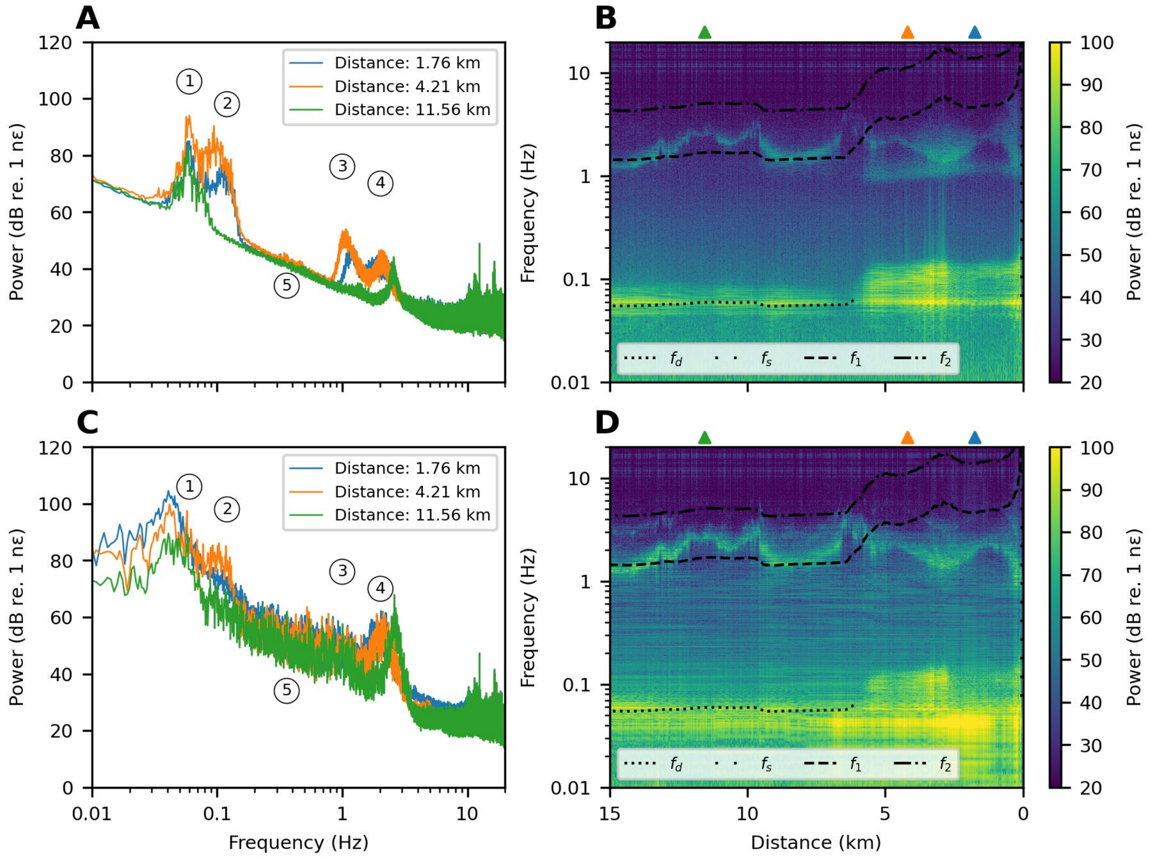

Figure 2. Spectral analysis of DAS strain data. The average power spectra at selected locations along the cable (**A**) and the power spectral profile (**B**) immediately before the earthquake, without strong seismic energy, computed from the 1200-s time window before 2020-07-22T06:20:02Z. The average power spectra at the same locations (**C**) and the power spectral profile (**D**) with seismic energy from the earthquake (P-, S- and SS-waves), computed from the 1200-s time window after 2020-07-22T06:20:02Z. The average power spectra in **A** and **C** are computed over 251 recording channels (500 m radius) around each location. The numeric annotations in **A** and **C** highlight key events discussed in the text. The colored triangles in **B** and **D** mark the locations associated with the power spectra in **A** and **C**. The frequency limits corresponding to ocean surface gravity waves with water depth >200 m (f_d) and with water depth <10 m (f_s), and normal modes (f_1 and f_2) are also plotted in **B** and **D**.

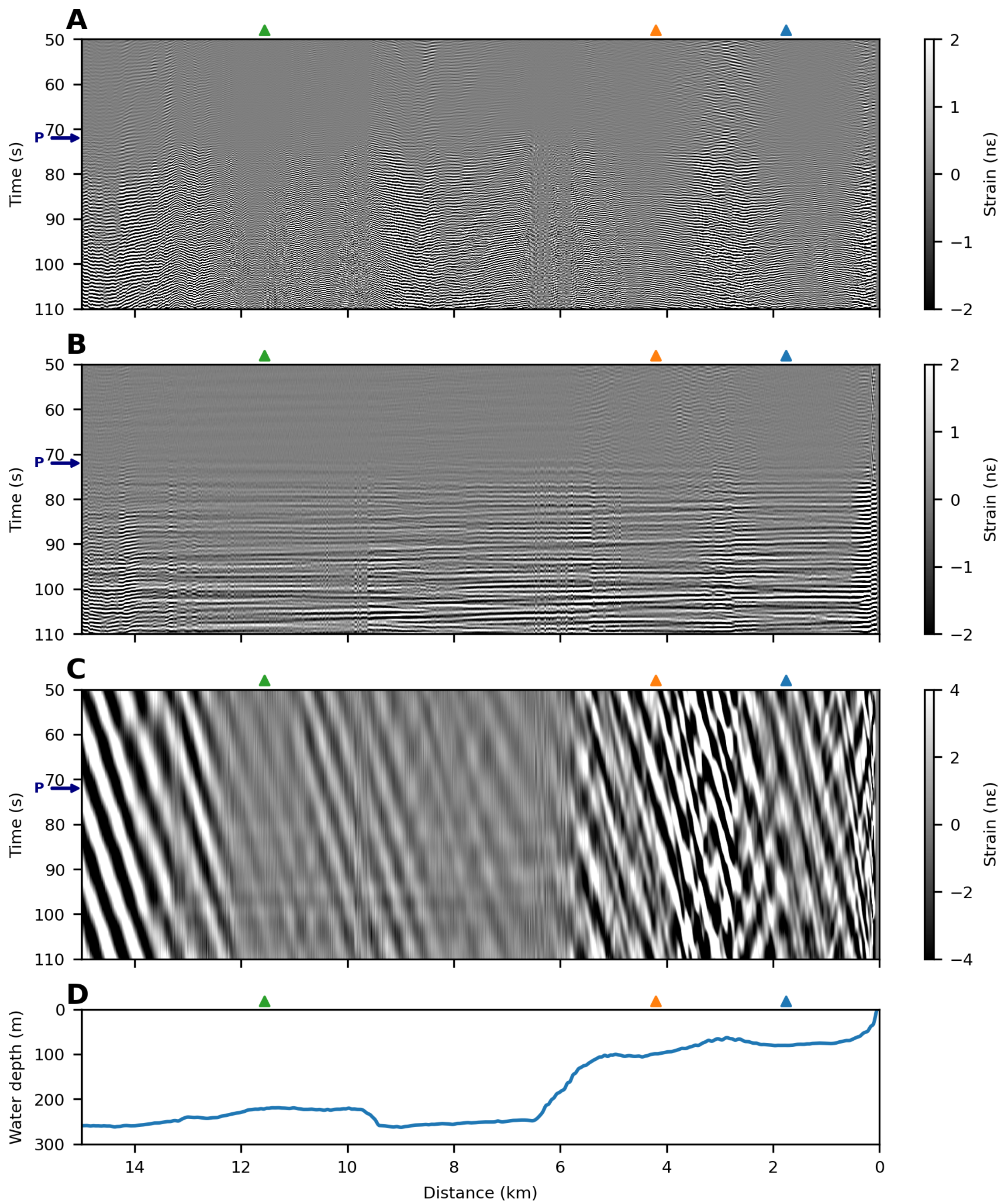

Figure 3. Band-limited DAS strain data. The strain data filtered to three frequency bands: **A** 1.2–20 Hz, **B** 0.2–1.2 Hz, and **C** 0.005–0.2 Hz. **D** The water depth profile. The recording time starts at 2020-07-22T06:20:02Z, after which the first P-wave from the 2020-07-22 M_{ww} 7.8 earthquake on the Alaska Peninsula arrives at about 72 s. The colored triangles mark the locations associated with the spectra shown in Figure 2.

The energy peak between 1.0 and 1.2 Hz (Event 3 in Figure 2A) also only exists in shallow water. We believe that it represents Scholte or other seismic waves that are excited locally in shallow water by ocean-bottom pressure variations as a result of ocean surface gravity waves. The last energy peak (Event 4 in Figure 2A) is associated with the fundamental acoustic resonance (f_1) of the water column, with frequency >1 Hz, varying with water depth. Note that this fundamental mode exists in all water depths for our DAS array.

In addition to the four features discussed above, there is a slight increase in energy around 0.36 Hz (Event 5 in Figure 2A) in the power spectra. An increase in energy around 0.36 Hz has been reported as the secondary microseism associated with the 0.18-Hz opposing surface gravity wave groups in a seabed DAS experiment in Belgium by Williams et al. (2019, fig. 2). In our data, we observe no energy peak around 0.18 Hz; hence, it is unlikely that the 0.36-Hz energy observed as Event 5 in Figure 2A is directly involved with ocean surface gravity waves. In addition, its frequency is not close to the frequency limits of ocean swells or acoustic resonance in the water column. Thus, we believe that Event 5 corresponds to hydrodynamic responses associated with seismic waves, although we cannot identify their seismic origins.

Figures 2C and 2D show the spectral analysis of DAS strain data that contain strong seismic waves (P-, S- and SS-waves) from the 2020-07-22 M_{ww} 7.8 earthquake on the Alaska Peninsula. Here, the responses caused by these seismic waves arriving at the seafloor significantly boost the strain power in the frequency range below 4 Hz. This energy is superimposed on the initial ambient levels shown in Figures 2A and 2B. Comparing the spectra with and without earthquake-related energy, we see that the energy peaks corresponding to primary and secondary microseisms (Events 1 and 2) have similar characteristics. We also observe no significant change to the Scholte wave response associated with ocean surface gravity waves (Event 3). In contrast, the water-layer acoustic resonance (Event 4) is enhanced, and its 2nd order mode is visible, when excited by the energy from the strong seismic waves. Therefore, we conclude that seismic waves from the earthquake propagate into the seawater, causing stronger acoustic resonance in the water column. The earthquake-related responses enhance the power spectra between 0.01 and 4 Hz, and their spectra have no correlation with water depth, as shown in Figures 2C and 2D. In addition, we observe that earthquake-related responses near the shore are stronger than in deeper water, which we suspect to be due to an amplitude attenuation effect from different subsurface rock types. Accordingly, all the energy peaks outside the frequency ranges of primary microseisms (Event 1), secondary microseisms (Event 2), Scholte waves (Event 3), and water-layer acoustic resonance (Event 4) are related to hydrodynamic responses from earthquakes. The responses discussed above have different characteristics in both temporal and spatial dimensions (see Figures S2 and S3 in Supporting Information for detailed analyses in the frequency-wavenumber and frequency-velocity domains).

The theoretical cut-off frequencies for the water-layer acoustic resonance shown in Figures 2B and 2D do not match the power spectral energy distribution, especially in shallow water at 0–6 km from shore. In shallow water, the frequency of the acoustic resonance, which ranges between 1 and 4 Hz, is lower than the corresponding theoretical cut-off frequency. This energy must therefore be evanescent or associated with acoustic resonance modes between the sea surface and a strong reflector below the seafloor soft sediments. The amplitude of evanescent waves typically decays rapidly. However, the energy peaks we observe have strong amplitudes. Therefore, they are unlikely associated with evanescent modes. We believe that these energy peaks are more likely related to propagating acoustic resonances, because their characteristics are similar to the acoustic resonances in deeper water, e.g., the higher order modes are enhanced by seismic waves from an earthquake. Thus, it is likely that these energy peaks in shallow water are caused by acoustic resonance between the sea surface and a strong reflector below the seafloor. A possible candidate is the Base of the Helvetiafjellet Formation which is approximately 200 m below the sea surface (Bælum et al., 2012, fig. 6). To explore this possibility, we would need detailed knowledge of the geological structure of this horizon, which is beyond the scope of this article.

Band-pass filtering the DAS strain data into three bands gives us the results illustrated in Figure 3, in which the first P-wave from the 2020-07-22 M_{ww} 7.8 earthquake on the Alaska Peninsula arrives at about 72 s. Therefore, Figure 3 reveals the characteristics of the seabed DAS data with and without earthquake-related responses.

Figure 3A shows the data in the frequency band from 1.2 to 20 Hz, which mostly comprise signals from water-column acoustic resonance (Event 4 in Figure 2). These responses are further enhanced after 72 s by the arrival of strong P-waves from the Alaska earthquake. In addition, the times of the acoustic resonance events shown in Figure 3A vary with water depth. Therefore, these events are not direct responses to the seismic P-waves, that are generally independent of water depth.

Figure 3B shows the data in the frequency band from 0.2 to 1.2 Hz. Here we see a series of strong P-waves from the Alaska earthquake arriving after 72 s. These P-waves are coherent and almost flat on the data profile. The direct signals from P-waves are independent of water depth. Note that we also observe weak P-waves before 72 s that represent seismic events from unknown sources that form a slight increase in energy around 0.36 Hz (Event 5 in Figure 2). We also see scattered events in shallow water (<100 m water depth) throughout the recording. These events represent Scholte waves or other seismic waves that are excited locally by ocean-bottom pressure variation due to ocean surface gravity waves (Event 3 in Figure 2).

In Figure 3C, the data in the frequency band from 0.005 to 0.2 Hz, we see right-dipping events all along the cable. These are primary microseisms corresponding to ocean surface gravity waves, propagating towards the shore (Event 1 in Figure 2). In addition, we observe left-dipping events near the shore where the water depth is <100 m, creating a ‘checkerboard’ pattern. These are ocean surface gravity waves that are reflected from the shoreface back to the ocean. The (non-linear) superposition of long-wavelength ocean surface gravity waves and their reflections in shallow water near the shore creates secondary microseisms (Event 2 in Figure 2). Based on our observation, the seismic waves from the earthquake do not change the characteristics of primary and secondary microseisms.

3.2 Ocean wave monitoring

Figure 4 shows spectrograms from selected DAS receivers at different water depths and distances from the shore. Figures 4A–C show the linear up-sweep trends of different primary microseism events ranging from 0.04 to 0.1 Hz. Their frequencies monotonically increase with time. These linear trends correspond to the ocean swells produced by distant storms. Over the entire period of recording, we identify 12 linear trends in the spectrograms. Most of them last between 50 and 100 hours, and can overlap in time and space. The amplitude level of these linear trends increases towards the inner parts of the fjord, i.e., the shore in Longyearbyen. Hence, the fjord appears to act as a ‘narrowing amplifier’ for the ocean swells produced by distant storms. In shallow water (Figure 4A), we observe stronger amplitudes of primary microseism signals, especially for the more locally-generated ones (with steeper gradients). While we do not expect to see secondary microseisms (at double the frequency of the primary microseism) in deep water (>100 m) at distances greater than 6 km on the DAS array, we do not see them even at 3.08 km along the cable, with an average water depth of 71 m. This is unexpected and remains to be understood. We believe that the secondary microseism should be strong enough to be seen in water depths <100 m.

Figure 4D shows the maximum speed of local winds measured at the Isfjord Radio and Svalbard Lufthavn weather stations near the DAS array. The Isfjord Radio station is located at the entrance of the fjord and close to the 55 km distance point along the DAS array, whereas Svalbard Lufthavn station is located at the Svalbard Airport in Longyearbyen and close to the start of the DAS array (see Figure 1C). We found no correlation between the local wind speeds and the primary microseisms associated with ocean swells. Therefore, we deduce that the primary microseisms visible in the spectrograms are mostly generated from winds or storms outside the fjord.

Four linear up-sweep trends of the primary microseisms corresponding to distant storms are highlighted in the spectrogram in Figure 4C. Using the methods described in the previous section, we can calculate the distance and time taken by the ocean swell to travel from each storm center to the DAS array. Table 1 summarizes the calculation of the four storms as marked in Figure 4C. By applying geographical and topological constraints (there must be an open seaway between our DAS array and the source) we can retrieve their approximate locations for comparison with public records. The Arctic Ocean is isolated from other oceans by land. The Fram Strait, which lies between Svalbard and Greenland, is the only deep passage into the Arctic Ocean. In addition, the main orientation of our DAS array points towards the Atlantic Ocean. Therefore, the primary microseisms detected by our DAS array are likely produced by storms in the Atlantic Ocean. It is unlikely that our DAS data are dominated by strong primary microseisms caused by storms in the Pacific Ocean through the shallow Bering Strait.

From public records, we can trace all the four linear trends in Figure 4C back to their corresponding storms in the Atlantic Ocean. Event 1 corresponds to the Tropical Storm Edouard near Bermuda at about 4,100 km away from Longyearbyen, occurring from 2020-07-04 to 2020-07-06 (Pasch, 2021). Event 2 possibly corresponds to the bomb cyclone in offshore south Brazil at about 13,000 km from Longyearbyen from 2020-06-30 to 2020-07-02 as reported in Gobato & Heidari (2020) and Khalid et al. (2020). According to weather news in Iceland (Ćirić, 2020), Event 3 should correspond to an extratropical depression between Iceland and Greenland at about 2,400 km away from the DAS array from 2020-07-15 to 2020-07-17. Lastly, Event 4 probably comes from a storm in a remote region in offshore south Brazil at about 11,000 km from the DAS array on 2020-07-12.

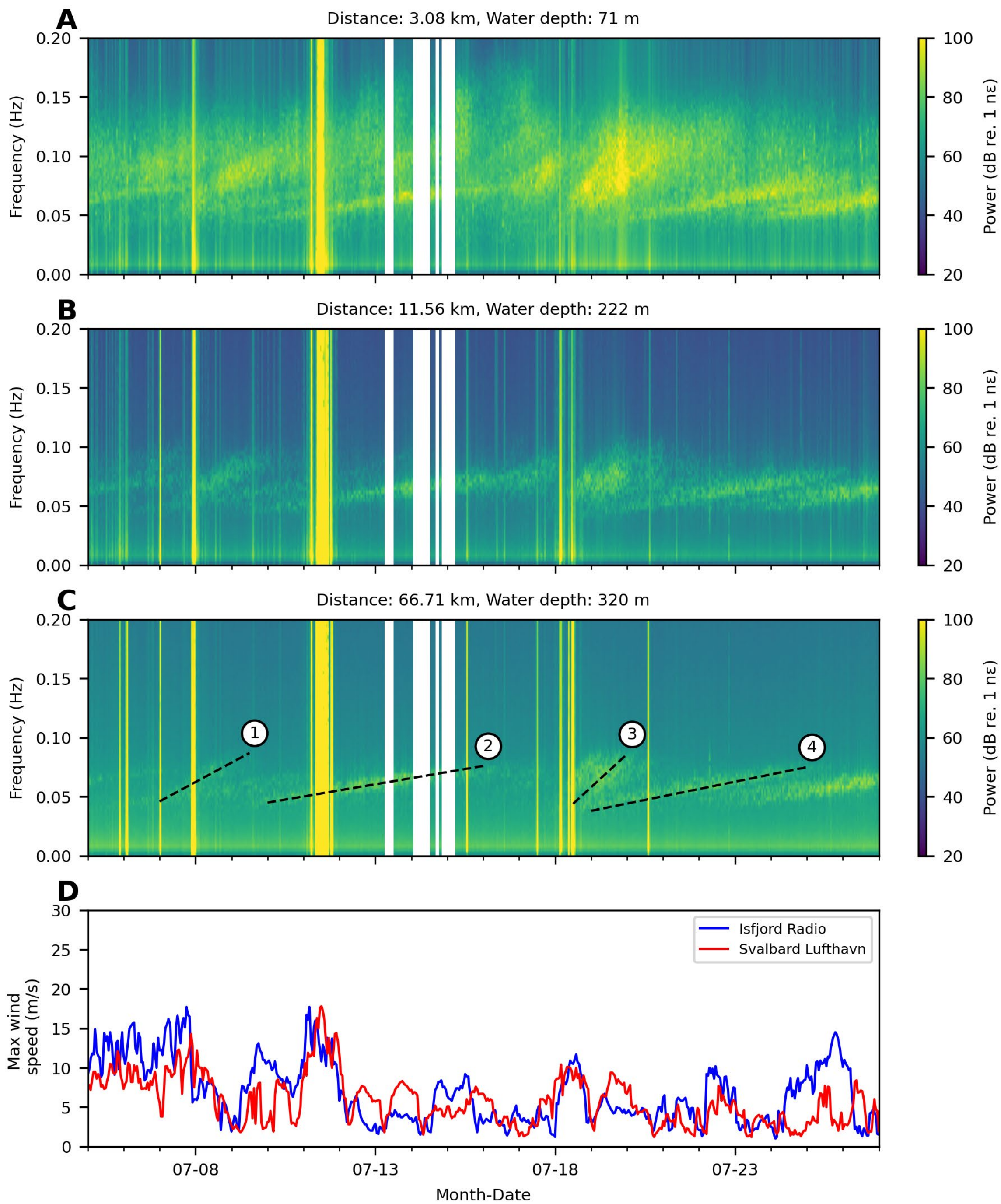

Figure 4. Spectrograms for storm monitoring. Spectrograms at 3.08 (**A**), 11.56 (**B**) and 66.71 (**C**) km along the DAS array from shore. Maximum wind speeds measured at Isfjord Radio and Svalbard Lufthavn weather stations (see Figure 1) are shown in **D**. Four storm events marked in **C** are discussed in the text. All the spectrograms are computed from the average power spectrum over 251 recording channels (500 m radius) around the selected locations within a 300-s time window on an hourly basis. In the spectrograms, the yellow vertical stripes are caused by dynamic range saturation, which is weakly correlated with the local storm noise from the winds illustrated in **D**, whereas the white vertical stripes indicate drop-out periods in the real-time data transfer.

Table 1. Estimated origins of the four ocean swells marked in Figure 4C.

Parameters	Event 1	Event 2	Event 3	Event 4
Start time at DAS (t_0)	2020-07-07 T00:00:00Z	2020-07-10 T00:00:00Z	2020-07-18 T12:00:00Z	2020-07-19 T00:00:00Z
End time at DAS (t_1)	2020-07-09 T12:00:00Z	2020-07-16 T00:00:00Z	2020-07-20 T00:00:00Z	2020-07-25 T00:00:00Z
Frequency at start time (f_0)	0.046 Hz	0.045 Hz	0.044 Hz	0.038 Hz
Frequency at end time (f_1)	0.087 Hz	0.076 Hz	0.086 Hz	0.075 Hz
Travel distance (x in equation (4))	4,113 km	13,055 km	2,409 km	10,938 km
Group velocity for the lowest-frequency swell (c_g in equation (5) with $f = f_0$)	16.97 m/s	17.35 m/s	17.74 m/s	20.54 m/s
Travel time for the lowest-frequency swell (t in equation (6))	67.32 hours	209.03 hours	37.71 hours	147.89 hours
Estimated time at source ($t_0 - t$)	2020-07-04 T04:40:00Z	2020-07-01 T06:58:00Z	2020-07-16 T22:17:00Z	2020-07-12 T20:06:00Z

3.3 Future oceanographic applications

Functioning marine ecosystems are vital to healthy oceans on which a sustainable future on Earth for all living beings ultimately depends (Danovaro et al., 2020). Marine acoustics plays an important role in studying physical processes in the oceans and their interaction with the solid earth, atmosphere and living organisms. Therefore, Passive Acoustic Monitoring (PAM) is recognized as an important surveillance tool for the Earth's ecosystems, through the studies of ocean ambient sound, marine mammal behavior, glacial/iceberg noise, anthropogenic ocean use, unsanctioned nuclear or other polluting activity, earthquake and tsunami warning, in addition to search and rescue.

We have shown that DAS, as a PAM system, can detect waves from various sources through dynamic interactions between the atmosphere, ocean, and solid earth. DAS has many valuable attributes to offer the oceanographic community, nicely complementing existing sensing systems such as satellites (which are broadly limited to very near-surface observations), buoys, moorings, and floats (which have limited spatial coverage and resolution). The advantages of DAS include broadband and high-resolution spatial and temporal measurement capacities, with data available in real-time to support active marine management and decision-making. The real-time capability, bringing data from the seafloor, is unmatched by any other system other than fixed installations cabled to shore or supporting long lines to surface buoys, both of which represent expensive and complex engineering challenges. The potential for earthquake and tsunami warning systems alone is therefore remarkable. This sensing network is also possible to create at low cost, since we can use existing submarine telecommunication cables. These cables span more than a million kilometers around all the oceans on the globe, potentially bringing a sensing capability to many less-sampled environments, and perhaps also able to support less developed countries in responsibly managing their maritime resources.

Thus, DAS brings an innovative and game-changing new sensing modality to oceanography and planetary observation systems in general. Therefore, we believe that DAS will become a valuable new component of the Global Ocean Observing System (GOOS), of the Intergovernmental Oceanographic Commission (IOC) of UNESCO, as discussed in Howe et al. (2019).

4 Conclusion

DAS in an ocean-bottom telecommunication cable can measure various types of ocean-bottom pressure responses that are caused by dynamics in the atmosphere, ocean, and solid earth. They comprise the responses from ocean surface gravity waves causing primary and secondary microseisms, Scholte waves, water-layer acoustic resonances, and seismic waves (P-, S- and SS-waves) from earthquakes. We clearly describe and compare their characteristics in the DAS data. Our interpretations are validated by redundant samples from the data acquired extensively in spatial and temporal dimensions, over 44 days along 120 km of a fiber-optic cable, which extends along the fjord across different water depths from 0 to 400 m. We observe primary microseisms from distant storms, their reflections from the shore in shallow water and the resulting non-linear wave-wave interaction, forming secondary microseisms. We also see an approximate correlation between hydroacoustic first mode energy and the theoretical cutoff, but this is not supported in the nearshore, shallow water, leading us to suspect that the energy may be associated with a mode resonating between the sea surface and a deeper rigid structure, rather than soft unconsolidated sediment. More detailed geological knowledge, beyond the scope of this paper, would be required to explore this possible explanation. The DAS data do enable us to trace several primary microseisms associated with ocean swells back to their storm origins, which are significant ocean-atmosphere disruptions occurring up to 13,000 km away. We also find that the fjord acts as a ‘narrowing amplifier’ for microseisms, because their amplitudes increase towards the inner parts of the fjord. Thus, it is possible to use DAS data acquired over 120 km to study dynamic interactions between the atmosphere, ocean, and solid earth. Thanks to its high spatial and temporal resolution, real-time data availability, broadband low frequency sensitivity and its ability to sense what is happening close to the seabed, capturing both hydroacoustic and seismic events, DAS offers great scientific value to Earth observation systems. We believe that DAS will become a key value sensing modality in the Global Ocean Observing System (GOOS).

Acknowledgments

The authors acknowledge the Research Council of Norway and the sponsors of the Geophysics and Applied Mathematics in Exploration and Safe production Project (GAMES; grant no. 294404), the Digimon ACT Project (grant no. 299622), and the Centre for Geophysical Forecasting (CGF; grant no. 309960) at NTNU for financial support. The authors thank Alcatel Submarine Networks Norway AS for supporting and operating the OptoDAS interrogator, and Uninett AS for providing access to their fiber-optic cable between Longyearbyen and Ny-Ålesund and operating the data transfer through their network between Svalbard and Trondheim. The authors thank Tim Cato Netland and Daniel Bergh for their technical support on the real-time data transfer.

Open research

DAS data for this research are available in Taweesintananon & Landrø (2022) via https://doi.org/10.18710/VPRD2H. Seismic data from the KBS seismic station in Svalbard used as our reference are available through IRIS web services: https://service.iris.edu/. Details on the 2020-07-22 M_{ww} 7.8 earthquake on the Alaska Peninsula are available at USGS web site: https://earthquake.usgs.gov/earthquakes/eventpage/us7000asvb/executive. The weather data are available through the Norwegian Center for Climate Services (NCCS) at https://seklima.met.no/observations/.

Author contributions

ML, SEJ, JKB, AH, OS and FS conceived and designed the experiment. AH and FS collected data. KT processed data and prepared the visualizations. KT and ML analyzed data with support from SEJ, JRP, RAR, LB and HJK. ML and JRP validated research outputs, acquired funding, and managed the project. KT wrote the original draft of the manuscript. All the authors conducted review & editing of the manuscript.

Competing interests

There is no competing interest related to this work.

References

Abolfazli, E., Liang, J., Fan, Y., Chen, Q. J., Walker, N. D., & Liu, J. (2020). Surface Gravity Waves and Their Role in Ocean-Atmosphere Coupling in the Gulf of Mexico. *Journal of Geophysical Research: Oceans*, *125*(7). https://doi.org/10.1029/2018JC014820

Airy, G. B. (1841). Tides and waves. In *Encyclopaedia Metropolitana (1817-1845)* (Vol. 3, pp. 241–396).

Ardhuin, F., & Herbers, T. H. C. (2013). Noise generation in the solid Earth, oceans and atmosphere, from nonlinear interacting surface gravity waves in finite depth. *Journal of Fluid Mechanics*, *716*, 316–348. https://doi.org/10.1017/jfm.2012.548

Bælum, K., Johansen, T. A., Johnsen, H., Rød, K., Ruud, B. O., & Braathen, A. (2012). Subsurface structures of the Longyearbyen CO2 Lab study area in Central Spitsbergen (Arctic Norway), as mapped by reflection seismic data. *Norwegian Journal of Geology*, *92*(4), 377–389.

Bigg, G. R., & Hanna, E. (2016). Impacts and effects of ocean warming on the weather. In D. Laffoley & J. M. Baxter (Eds.), *Explaining ocean warming: Causes, scale, effects and consequences* (pp. 359–372). International Union for Conservation of Nature and Natural Resources (IUCN). http://dx.doi.org/10.2305/IUCN.CH.2016.08.en

Bromirski, P. D., & Duennebier, F. K. (2002). The near-coastal microseism spectrum: Spatial and temporal wave climate relationships. *Journal of Geophysical Research: Solid Earth*, *107*(B8), ESE 5-1--20. https://doi.org/10.1029/2001JB000265

Ćirić, J. (2020, July 15). Weather Warning for Central Highland, Northwest Iceland [News]. *Iceland Review*. https://www.icelandreview.com/travel/weather-warning-for-central-highland-northwest-iceland/

Craik, A. D. D. (2004). The origins of water wave theory. *Annual Review of Fluid Mechanics*, *36*(1), 1–28. https://doi.org/10.1146/annurev.fluid.36.050802.122118

Danovaro, R., Fanelli, E., Aguzzi, J., Billett, D., Carugati, L., Corinaldesi, C., Dell'Anno, A., Gjerde, K., Jamieson, A. J., Kark, S., McClain, C., Levin, L., Levin, N., Ramirez-Llodra, E., Ruhl, H., Smith, C. R., Snelgrove, P. V. R., Thomsen, L., Van Dover, C. L., & Yasuhara, M. (2020). Ecological variables for developing a global deep-ocean monitoring and conservation strategy. *Nature Ecology & Evolution*, *4*(2), 181–192. https://doi.org/10.1038/s41559-019-1091-z

Dean, R. G., & Dalrymple, R. A. (1991). *Water Wave Mechanics for Engineers and Scientists: Vol. Volume 2*. WORLD SCIENTIFIC. https://doi.org/10.1142/1232

European cooperation in science and technology Action 714, Working Group 3. (2005). *Measuring and analysing the directional spectra of ocean waves* (D. Hauser, H. Krogstad, & K. Kahma, Eds.). EU Publications Office. http://dx.doi.org/10.25607/OBP-811

Gobato, R., & Heidari, A. (2020). Cyclone Bomb Hits Southern Brazil in 2020. *Journal of Atmospheric Science Research*, *3*(3), 8–12. https://doi.org/10.30564/jasr.v3i3.2163

Hartog, A. H. (2017). *An Introduction to Distributed Optical Fibre Sensors* (1st ed.). CRC Press. https://doi.org/10.1201/9781315119014

Hasselmann, K. (1963). A statistical analysis of the generation of microseisms. *Reviews of Geophysics*, *1*(2), 177. https://doi.org/10.1029/RG001i002p00177

Howe, B. M., Miksis-Olds, J., Rehm, E., Sagen, H., Worcester, P. F., & Haralabus, G. (2019). Observing the Oceans Acoustically. *Frontiers in Marine Science*, *6*, 426. https://doi.org/10.3389/fmars.2019.00426

Khalid, A., de Lima, A. de S., Cassalho, F., Miesse, T., & Ferreira, C. (2020). Hydrodynamic and Wave Responses During Storm Surges on the Southern Brazilian Coast: A Real-Time Forecast System. *Water*, *12*(12), 3397. https://doi.org/10.3390/w12123397

Landrø, M., Bouffaut, L., Kriesell, H. J., Potter, J. R., Rørstadbotnen, R. A., Taweesintananon, K., Johansen, S. E., Brenne, J. K., Haukanes, A., Schjelderup, O., & Storvik, F. (2021). Title: Sensing whales, storms, ships and earthquakes using an Arctic fibre- optic cable. *Earth and Space Science Open Archive*, 39. https://doi.org/10.1002/essoar.10507855.1

Landrø, M., & Hatchell, P. (2012). Normal modes in seismic data—Revisited. *GEOPHYSICS*, *77*(4), W27–W40. https://doi.org/10.1190/geo2011-0094.1

Lin, J., Fang, S., Li, X., Wu, R., & Zheng, H. (2018). Seismological Observations of Ocean Swells Induced by Typhoon Megi Using Dispersive Microseisms Recorded in Coastal Areas. *Remote Sensing*, *10*(9), 1437. https://doi.org/10.3390/rs10091437

Lindsey, N. J., Dawe, T. C., & Ajo-Franklin, J. B. (2019). Illuminating seafloor faults and ocean dynamics with dark fiber distributed acoustic sensing. *Science*, *366*(6469), 1103–1107. https://doi.org/10.1126/science.aay5881

Matsumoto, H., Inoue, S., Ohmachi, T., Japan Agency for Marin-Earth Science and Technology, 2-15 Natsushima, Yokosuka 237-0061, Japan, Takenaka Research and Development Institute, 1-5-1 Ohtsuka, Inzai, Chiba 270-1395, Japan, & Japan Dam Engineering Center, Nissyoku Bld., 2-9-7 Ikenohata, Taito, Tokyo 110-0008, Japan. (2012). Dynamic Response of Bottom Water Pressure due to the 2011 Tohoku Earthquake. *Journal of Disaster Research*, *7*(sp), 468–475. https://doi.org/10.20965/jdr.2012.p0468

Mitsuyasu, H. (2002). A Historical Note on the Study of Ocean Surface Waves. *Journal of Oceanography*, *58*(1), 109–120. https://doi.org/10.1023/A:1015880802272

Munk, W. H. (1950). On the wind-driven ocean circulation. *Journal of Atmospheric Sciences*, *7*(2), 80–93. https://doi.org/10.1175/1520-0469(1950)007<0080:OTWDOC>2.0.CO;2

Munk, W. H., Miller, G. R., Snodgrass, F. E., Barber, N. F., & Deacon, G. E. R. (1963). Directional recording of swell from distant storms. *Philosophical Transactions of the Royal Society of London. Series A, Mathematical and Physical Sciences*, *255*(1062), 505–584. https://doi.org/10.1098/rsta.1963.0011

Pasch, R. J. (2021). *National hurricane center tropical cyclone report: Tropical storm Edouard (AL052020)* (pp. 1--11) [Technical report]. National Oceanic and Atmospheric Administration. https://www.nhc.noaa.gov/data/tcr/AL052020_Edouard.pdf

Saito, T., & Tsushima, H. (2016). Synthesizing ocean bottom pressure records including seismic wave and tsunami contributions: Toward realistic tests of monitoring systems. *Journal of Geophysical Research: Solid Earth*, *121*(11), 8175–8195. https://doi.org/10.1002/2016JB013195

Schmitt, R. W. (2018). The ocean's role in climate. *Oceanography*, *31*(2), 32–40. https://doi.org/10.5670/oceanog.2018.225

Sladen, A., Rivet, D., Ampuero, J. P., De Barros, L., Hello, Y., Calbris, G., & Lamare, P. (2019). Distributed sensing of earthquakes and ocean-solid Earth interactions on seafloor telecom cables. *Nature Communications*, *10*(1), 5777. https://doi.org/10.1038/s41467-019-13793-z

Stommel, H. (1948). The westward intensification of wind-driven ocean currents. *Eos, Transactions American Geophysical Union*, *29*(2), 202–206. https://doi.org/10.1029/TR029i002p00202

Sverdrup, H. U. (1947). Wind-Driven Currents in a Baroclinic Ocean; with Application to the Equatorial Currents of the Eastern Pacific. *Proceedings of the National Academy of Sciences*, *33*(11), 318–326. https://doi.org/10.1073/pnas.33.11.318

Taweesintananon, K., & Landrø, M. (2022). *Replication data for DAS4Microseism—Svalbard distributed acoustic sensing (DAS) strain data for oceanographic study* (Norwegian University of Science and Technology, Ed.). DataverseNO. https://doi.org/10.18710/VPRD2H

Villas Bôas, A. B., Ardhuin, F., Ayet, A., Bourassa, M. A., Brandt, P., Chapron, B., Cornuelle, B. D., Farrar, J. T., Fewings, M. R., Fox-Kemper, B., Gille, S. T., Gommenginger, C., Heimbach, P., Hell, M. C., Li, Q., Mazloff, M. R., Merrifield, S. T., Mouche, A., Rio, M. H., … van Sebille, E. (2019). Integrated Observations of Global Surface Winds, Currents, and Waves: Requirements and Challenges for the Next Decade. *Frontiers in Marine Science*, *6*, 425. https://doi.org/10.3389/fmars.2019.00425

Waagaard, O. H., Rønnekleiv, E., Haukanes, A., Stabo-Eeg, F., Thingbø, D., Forbord, S., Aasen, S. E., & Brenne, J. K. (2021). Real-time low noise distributed acoustic sensing in 171 km low loss fiber. *OSA Continuum*, *4*(2), 688–701. https://doi.org/10.1364/OSAC.408761

Williams, E. F., Fernández-Ruiz, M. R., Magalhaes, R., Vanthillo, R., Zhan, Z., González-Herráez, M., & Martins, H. F. (2019). Distributed sensing of microseisms and teleseisms with submarine dark fibers. *Nature Communications*, *10*(1), 5778. https://doi.org/10.1038/s41467-019-13262-7

Wu, L., Breivik, Ø., & Rutgersson, A. (2019). Ocean-Wave-Atmosphere Interaction Processes in a Fully Coupled Modeling System. *Journal of Advances in Modeling Earth Systems*, *11*(11), 3852–3874. https://doi.org/10.1029/2019MS001761

Wunsch, C. (2021). The Rise of Dynamical Oceanography—A Fragmentary Historical Note: The Stommel-Munk Correspondence, 1947–1953. *Oceanography*, *34*(1), 249–253. https://doi.org/10.5670/oceanog.2021.101

Zhan, Z., Cantono, M., Kamalov, V., Mecozzi, A., Müller, R., Yin, S., & Castellanos, J. C. (2021). Optical polarization–based seismic and water wave sensing on transoceanic cables. *Science*, *371*(6532), 931–936. https://doi.org/10.1126/science.abe6648